Chirality Induced Pair Breaking in Type 2 Superconductors

Author: Alexander Rommens (s3678865)

Daily supervisor: Prof. Dr. A. Higginbotham
First examiner: Prof Dr. C. H. van der Wal
Second Examiner: Prof Dr. B. van Wees

August 2022

Abstract

This thesis details the theoretical framework and experimental realization of a hybrid quantum system coupling chiral molecules and type 2 superconductors. By utilizing coplanar waveguide resonators and transport measurements the superfluid density was probed through the shifting resonant frequency and fit to BCS theory. The pair-breaking response to increasing temperature and applied magnetic fields was used to gain insight into the behaviour of the adsorbed molecules and their contribution to the destruction of Cooper pairs. Due to additional effects from vortex formation and systematic errors in the data, the pair-breaking role of molecules could not be definitively determined. The potential emergence of triplet superconductivity upon adsorption was also explored in the low-temperature regime with a possible deviation from BCS theory identified.

CONTENTS

I. ACKNOWLEDGEMENTS

This research was carried out as an international collaboration between the Institute of Science and Technology Austria and the University of Groningen. The experimental work was carried out in the lab of Professor Andrew Higginbotham under his supervision.

II. INTRODUCTION

Over the last few decades, the consistent improvement in spintronic and quantum computing platforms has led to increasing useful systems and bold predictions for future applicability. However, for these systems to become viable contenders against classical computing architectures radical change is needed. The prospect of combining techniques to build hybrid quantum systems capable of more than the sum of their parts has led to practical developments from better-protected qubits to advances in quantum transduction. Given experimental access to triplet superconductivity, several promising research directions may become more accessible including superconducting spintronics and topological quantum computing.

The current set of candidate materials for triplet superconductivity suffer from a series of fundamental flaws holding back wide-scale applications. Materials based around single crystals such as UTe_2 [1] must be integrated into circuits and interfaced with, introducing complexity to planar designs. Using a ferromagnetic/superconductor interface to generate triplet pairing also requires a ferromagnet in close proximity to the superconducting circuit potentially introducing loss and unwanted magnetic fields [2]. The coupling of chiral molecules and Type 2 superconductors may offer a method to induce unconventional superconductivity through a simple surface treatment bypassing the need to introduce new materials. While a modification of the order parameter due to chiral induced spin selectivity (CISS) is still debated and more research is needed to definitively claim the emergence of unconventional superconductivity such a technique may aid in developing triplet devices with existing scalable architectures.

Throughout this thesis two main questions will be investigated: can adsorbed chiral molecules be modelled as magnetic impurities on a conventional superconductor and is there evidence for triplet pairing in low-temperature measurements of the coupled system? The experimental characterization of the type 2 superconductor - chiral molecule system is thus broken into two major pathways:

1) The pair breaking response due to high temperatures and high fields from which the presence of magnetic impurities can be identified.

2) The low-temperature superfluid density response indicating potential deviations from conventional superconductivity.

The role of vortices in the Type 2 superconductor and their contributions to the data will also be qualitatively explored and solutions proposed to mitigate their effects.

III. SUPERCONDUCTIVITY

The formation and destruction of Cooper pairs in Bardeen-Cooper-Schrieffer (BCS) theory provides a theoretical framework to understand how external perturbations affect the superconducting condensate. The role of time reversal symmetry in the formation of pairs and the effects of breaking it are explored in the context of chiral molecules. As a prelude, several characteristic length scales are introduced to describe the penetration of magnetic fields, variation in the superfluid density and scattering of electrons in order to approximate the superconducting behaviour.

A. Macroscopic Description

Phase transitions often lead to dramatic changes in the macroscopic characteristics of a system. Under specific conditions, some materials can undergo a second-order phase transition to enter a superconducting state. Superconductivity is broadly characterized by zero resistance and the expulsion of magnetic flux or perfect diamagnetism. The London equations were proposed to phenomenologically describe these effects through [3]:

$$\frac{d\mathbf{J}_s}{dt} = \frac{n_s e^2}{m}\mathbf{E} \ , \qquad \nabla \times \mathbf{J}_s = -\left(\frac{\mu_0 n_s e^2}{m}\right)\mathbf{H} \tag{1}$$

An expression for flux penetration can be obtained from the Maxwell and London equations as:

$$\nabla^2\mathbf{H} + \frac{1}{\lambda_L^2}\mathbf{H} = 0 \implies \mathbf{H}(x) = \mathbf{H}(0)e^{-x/\lambda_L} \tag{2}$$

With $\mathbf{H}(0)$ the applied parallel field and λ_L the London penetration depth; a length scale describing the exponential decay of flux in a superconductor, useful for understanding field penetration [4]:

$$\lambda_L = \left(\frac{m}{\mu_0 n_s e^2}\right)^{1/2} \tag{3}$$

It could also be seen that at a critical temperature T_c and critical field H_c superconductivity was destroyed, indicating a deeper mechanism underlying the phenomenological theory.

B. Microscopic Description

The characteristic properties of superconductivity arise from the microscopic interactions between electrons and the lattice at low temperatures. As an electron traverses the lattice it distorts the surrounding ions from their original positions leading to an overall positive charge in its wake. Through attraction to this region by a second electron, the lattice effectively mediates an attractive interaction. This response can be quantized as an electron-phonon interaction resulting in an attractive potential [4]. The formation of a bound state between two electrons in the presence of even a weak attractive interaction was shown by Cooper et al. [5] The corresponding binding energy represents the energy cost required to overcome the attractive potential:

$$E_g(0) = 2\Delta(0) = 3.53 k_B T_c \tag{4}$$

The bound state is composed of two electrons of opposite spin and is defined as a Cooper pair. Cooper pairs are equivalently described as time-reversed electron states in accordance with Kramer's degeneracy theorem and can be seen as the charge carriers in a superconductor.

C. The BCS Ground State and Superconducting Gap

In a normal metal available states are consecutively filled to the Fermi energy in accordance with the Pauli exclusion principle. The bound nature of Cooper pairs modifies the physics responsible for this Fermi sea. Rather than being seen as separate particles, a cooper pair can be modelled as a quasi-particle with integer spin. This bosonic picture disrupts the fermionic degeneracy of electrons and allows for the condensation of many particles to a single degenerate ground state.

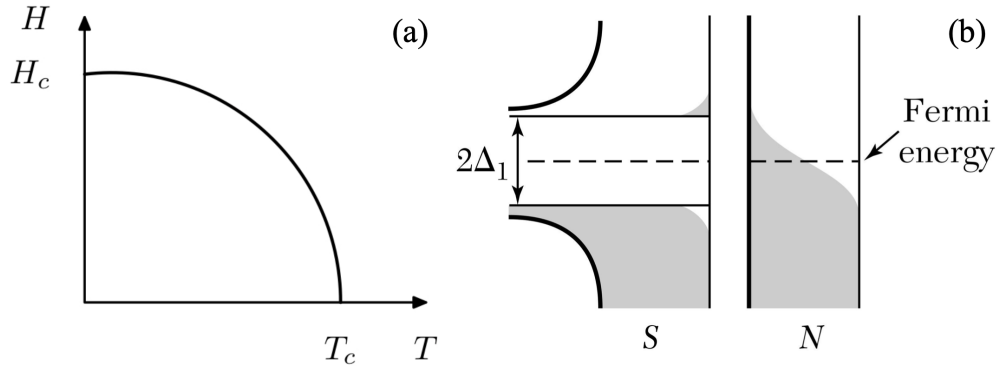

Fig. 1: (a) Superconducting phase diagram illustrating the critical field and critical temperature [3], (b) formation of the superconducting gap around the Fermi energy and distribution of excited states [6].

The energy spectrum around the ground state is dramatically changed by the condensation of Cooper pairs. An energy gap 2Δ is established around the Fermi energy that closes at the critical temperature, with a temperature dependence [4]:

$$\Delta(T) = 1.74\Delta(0)\left(1 - \frac{T}{T_c}\right)^{1/2} \tag{5}$$

The spatial extent of the superfluid condensate can be described through the coherence length ξ_0 and expressed in terms of the Fermi velocity and gap as [4]:

$$\xi_0 = \frac{\hbar v_F}{\pi\Delta(0)} \tag{6}$$

The coherence length characterizes the length scale of variations in the superfluid density.

D. The Dirty Limit

Superconducting behaviour can be approximated based on the purity of the material, quantified through the mean free path. An expression for ℓ can be determined from electron conduction [6]:

$$\sigma = \frac{ne^2\ell}{mv_F} \tag{7}$$

The dirty limit is defined when $\xi_0 \gg \ell$ and can be used to approximate the behaviour of Type 2 superconductors. In the dirty limit the temperature-dependent penetration depth and coherence length can be expressed as [4]:

$$\lambda(T) = 0.62\lambda_L\left(\frac{\xi_0}{\ell}\right)^{1/2}\left(\frac{T_c}{T_c - T}\right)^{1/2} \qquad \xi(T) = 0.85(\xi_0\ell)^{1/2}\left(\frac{T_c}{T_c - T}\right)^{1/2} \tag{8}$$

IV. EXOTIC FLAVOURS OF SUPERCONDUCTIVITY

A. *Type 2 Superconductors*

Superconductors can be organized into two broad categories based on their response to magnetic fields. Type 1 materials are characterized by the complete expulsion of magnetic flux up to a critical field H_c followed by the discontinuous breakdown of superconductivity. In contrast, Type 2 materials exhibit perfect diamagnetism up to a lower critical field H_{c1} before flux begins to penetrate the material without completely destroying its properties. The ratio of λ and ξ, the Ginzburg-Landau parameter, can be used to differentiate the types [4]:

$$\kappa = \frac{\lambda(T)}{\xi(T)} \implies \begin{cases} 0 < \kappa < \frac{1}{\sqrt{2}} & \text{Type 1} \\ \kappa > \frac{1}{\sqrt{2}} & \text{Type 2} \end{cases} \tag{9}$$

Equations 3, 7, 8 and 9 can be used to approximate κ in the dirty limit in terms of the sheet resistance $R_\square = 1/\sigma t$ and electron diffusion constant $D = \frac{1}{3} v_F \ell$:

$$\kappa = 0.715 \left(\frac{\lambda_L}{\ell}\right) = 0.715 \left(\frac{R_\square t}{3\mu_0 D}\right) \tag{10}$$

If $\kappa > 1/\sqrt{2}$ the free energy at the superconductor-metal interface becomes negative and it becomes energetically favourable for flux tubes to form through which the field can penetrate. These Abrikosov vortices are composed of a non-superconducting core surrounded by a circulating supercurrent that screens the internal field from the superconductor [3].

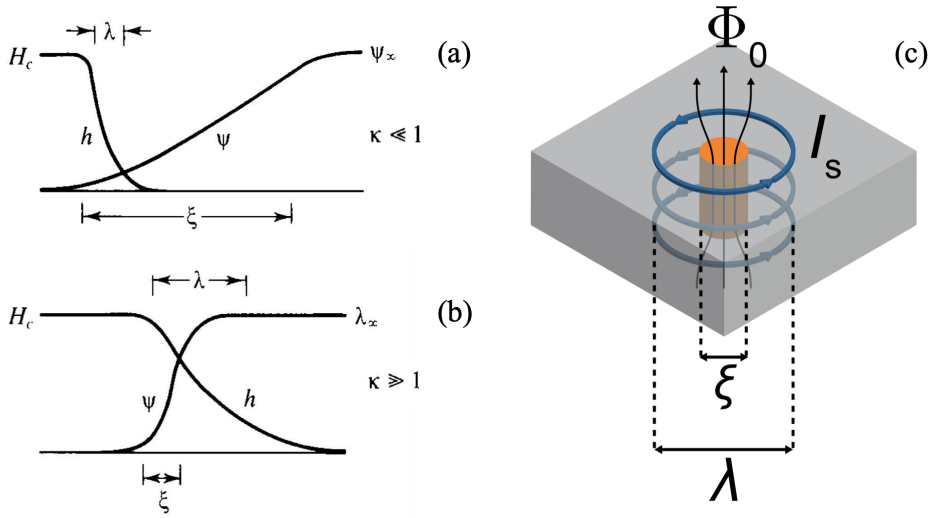

Fig. 2: (a), (b) The relationship between the penetration depth and coherence length in type 1 and type 2 superconductors [4]. (c) A schematic of an Abrikosov vortex illustrating the circulating supercurrent and role of the length scales in its formation [7].

The field at which vortices form H_{c1} can be expressed in terms of H_{c2} and κ as [4]:

$$H_{c1} = \frac{H_c}{\sqrt{2}\kappa} \ln(\kappa) = \frac{H_{c2}}{2\kappa^2} \ln(\kappa) \tag{11}$$

Vortices can move throughout the superconductor leading to loss through scattering events with charge carriers. Vortices can be pinned by inhomogeneities in the film or artificial defect sites to reduce the number that forms and control the ones that do [7], [8].

B. S-Wave and P-Wave Superconductivity

The symmetry of Cooper pairs allows for an additional classification scheme to be introduced. The superconducting materials discussed thus far exhibit s-wave superconductivity characterized by paired spins existing in a singlet state with even spatial parity. S-wave pairing originates from the electron-phonon interaction described by BCS theory. In contrast, p-wave superconductors can form Cooper pairs in a triplet state with odd parity under spatial inversion. Such triplet states originate from unconventional pairing mechanisms beyond the lattice interaction [9].

TABLE I: Characteristics of s-wave, p-wave and d-wave superconductivity. D-wave pairing is mentioned for the sole purpose of differentiating it from p-wave [9].

Type	Angular Momentum (L)	Spatial Parity	Spin Pairing
s-wave	0	Even	Singlet
p-wave	1	Odd	Triplet
d-wave	2	Even	Singlet

There are several relevant techniques to experimentally identify triplet superconductivity. In scanning tunnelling microscopy p-wave pairing exhibits a zero bias conduction peak that does not split with the applied field allowing for differentiation from s-wave/d-wave materials [10].

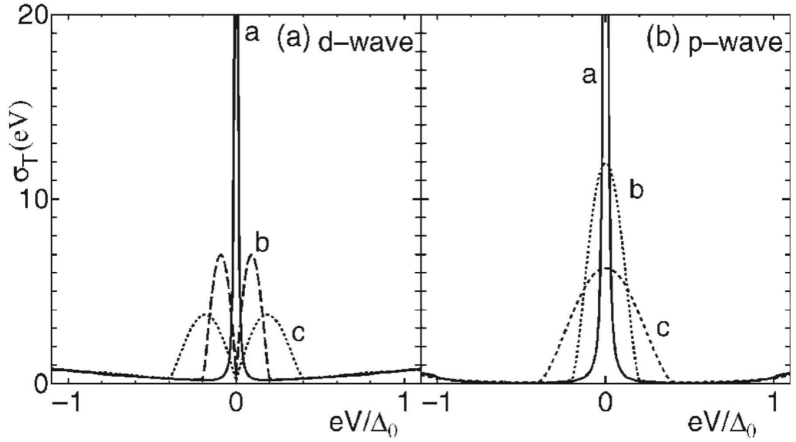

Fig. 3: (a) Zero bias conduction peak due to d-wave pairing. (b) Zero bias conduction peak due to p_x-wave pairing. The three curves on each plot a-c represent increasing magnetic field [10].

The temperature-dependent superfluid density of a p-wave superconductor also deviates from conventional s-wave behaviour [11]. The p-wave response is complex, anisotropic and reminiscent of d-wave but can be used as an indication of unconventional pairing.

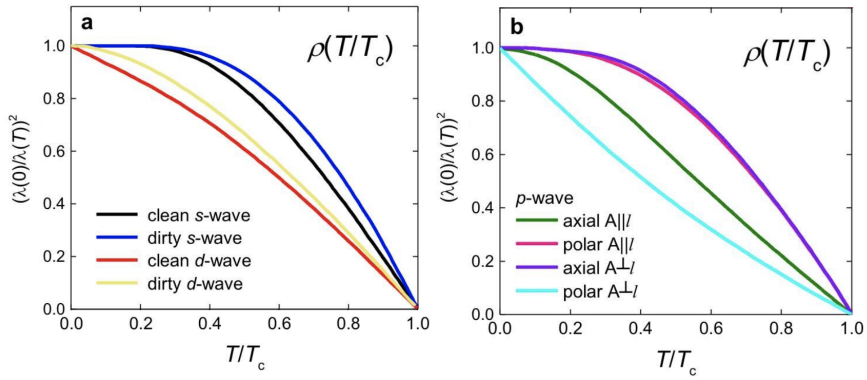

Fig. 4: Normalized temperature dependent superfluid density for s-wave, d-wave and p-wave superconductors [11].

V. CHIRAL HELICAL MOLECULES

The chiral structure of certain molecules can lead to the violation of time reversal symmetry dramatically affecting the behaviour of electrons and leading to novel emergent properties. This interaction conceived as chiral induced spin selectivity (CISS) is characterized by spin-polarized electron transport through the molecule and the magnetization of ferromagnetic substrates [12].

A. CISS Effect

The full mechanism for the CISS effect is not fully understood with significant debate about its origin and the magnitude of the interaction. However, several fundamental principles can be stated. Namely, by breaking time-reversal symmetry Kramer's degeneracy theorem no longer holds and a net spin polarization becomes possible. The CISS effect also relies on a spin-flip electron reflection process in the linear regime [12] in analogy with magnetic impurities.

B. Proximity Effects

Over the last decade, a wide body of experimental research has been developed investigating the secondary phenomena the CISS effect produces in superconductors upon adsorption. However, as the general principle behind the effect remains in debate it has proven difficult to attribute these results to a single mechanism. The impact of chiral molecules on the local density of states of Niobium was investigated through the use of scanning tunnelling microscopy [13]. The resulting conductance spectra exhibited a ZBCP and required an order parameter with both an s-wave and p-wave contribution to be accurately fit. The deviation from pure s-wave behaviour is notable and indicative of an interaction with the superconducting condensate.

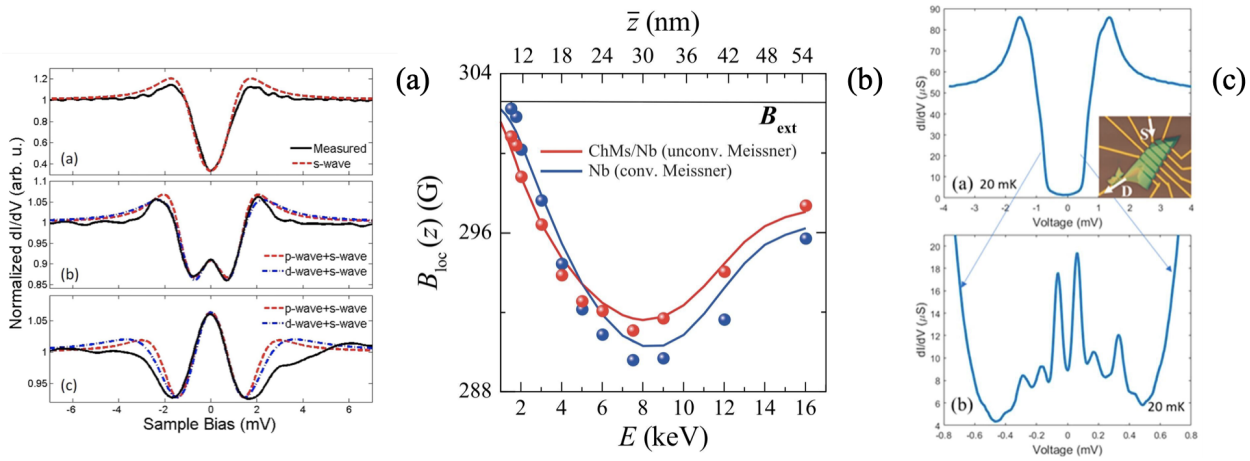

Fig. 5: (a) Emergence of ZBCP before and after molecule adsorption [13], (b) unconventional Meissner screening determined from muon spectroscopy [14], (c) formation of YSR states in the gap attributed to magnetic impurities [15].

The possibility of triplet pairs forming due to adsorbed molecules was further indicated through zero-field muon spin spectroscopy measurements [14]. Upon adsorption, the muon response suggested the emergence of unconventional Meissner screening on the scale of ξ_0 and bulk effects due to the modification of the order parameter by a p-wave component, figure 5 (b). In related work [15], the conductance spectra of $NbSe_2$ flakes illustrated both the emergence of ZBCPs and a secondary phenomenon with a split ZBCP. This split peak was attributed to the molecules acting as magnetic impurities and leading to the formation of impurity states in the superconducting gap, figure 5 (c). These results paint a mixed picture with the possibility of adsorbed molecules leading to both a mixed s-wave/p-wave order parameter and acting as magnetic impurities. The emergence of d-wave singlet states should also be considered given the ambiguity.

VI. PAIR BREAKING

The response of Cooper pairs to temperature, applied field and magnetic impurities yields a set of theoretical predictions for evaluating data and extracting information. BCS theory provides the framework to understand how bound states break in thin superconducting films allowing for deviations to be determined and potentially attributed to unconventional superconductivity.

A. Kinetic Inductance

As Cooper pairs have a non-zero mass they experience an inertial force in response to an alternating current. This results in a phase lag and inductive impedance in the superconductor that can be quantified through the kinetic inductance of the Cooper pairs:

$$U = \frac{1}{2} L_K I^2 \tag{12}$$

Equivalently, the kinetic inductance represents the energy stored in the kinetic energy of Cooper pairs and can be expressed in terms of supercurrent density $J_s = n_s e v_s$:

$$U = \frac{1}{2} n_s m v_s^2 = \frac{1}{2} \left(\frac{m J_s^2}{e^2 n_s} \right) \tag{13}$$

Combining equations 12, 13 yields an inverse relationship between superfluid density and kinetic inductance [16]. Pair breaking increases the kinetic inductance through a modification of n_s:

$$L_K \propto n_s^{-1} \tag{14}$$

B. Temperature Dependence

With an increase in temperature, Cooper pairs begin to break leading to a proliferation of thermally excited quasiparticles. The temperature-dependent kinetic inductance can be represented from BCS theory in terms of the material's sheet resistance, geometry, and superconducting gap [17]:

$$L_K(T) = \left(\frac{\ell}{w} \right) \left(\frac{R_\square}{2\pi^2 \Delta(T)} \right) \left[\tanh \left(\frac{\Delta(T)}{2 k_B T} \right) \right]^{-1} \tag{15}$$

Given that the critical temperature and sheet resistance are known this provides a BCS prediction for temperature-dependent pair breaking through L_K and a check on measurements of field-dependent pair breaking.

C. The Pair Breaking Coefficient

As Cooper pairs can be seen as time-reversed states any interaction that acts inconsistently on the partners will destabilize the bound state. Generally, pair breaking can be expressed in terms of the pair breaking coefficient α rather than the kinetic inductance. Wherein a pair-breaking ergodic perturbation results in an energy difference 2α between the time-reversed states [4]. In the dirty limit and for small α, the pair breaking coefficient can be approximated through ΔT_c:

$$\alpha = -\frac{4 k_B \Delta T_c}{\pi} \tag{16}$$

The presence of multiple pair-breaking perturbations can be represented additively through α.

D. Magnetic Field Dependence

Applied magnetic fields interact with the magnetic dipole moments μ_s of electrons resulting in Zeeman splitting. This dynamical process is odd under time-reversal symmetry and thus contributes to the breaking of Cooper pairs into quasiparticles. According to BCS theory the pair breaking coefficient of a thin film in a parallel magnetic field has a quadratic dependence on B [4]:

$$\alpha(B_{\parallel}) = \frac{1}{6}\left(\frac{De^2d^2}{\hbar}\right)B_{\parallel}^2 \tag{17}$$

Where D is the electronic diffusion constant, dependent on the mean free path $D = \frac{1}{3}v_F\ell$. In a perpendicular field the orbital effect dominates over the Zeeman effect resulting in a pair breaking coefficient linear in the field [4]:

$$\alpha(B_{\perp}) = \big(De\big)B_{\perp} \tag{18}$$

When combined with equation 16 the expressions for ΔT_c can be used to determine the change in resonant frequency Δf_r due to field-dependent pair breaking.

E. Magnetic Impurities

The presence of magnetic impurities introduces an additional term to field-dependent pair breaking. Time reversal symmetry is broken through a spin-orbit-dependent scattering process that culminates in a spin flip. The pair breaking coefficient can be approximated as [4]:

$$\alpha \approx \left(\frac{\tau_{so}e^2\hbar}{2m^2c^2}\right)B_{\parallel}^2 \tag{19}$$

Where τ_{so} is the scattering time associated with the spin-orbit interaction. Given the time-reversal symmetry-breaking nature of the CISS effect, the adsorption of chiral molecules to the superconductor is expected to result in an additional term in the pair-breaking response. However, as the molecules are nonmagnetic in isolation it is unclear if the pair breaking term can be modelled through the atomic magnetic impurity result above.

F. Pair Breaking in a Triplet Superconductor

The above expressions for the pair breaking coefficient are valid for conventional BCS s-wave superconductors. In a triplet superconductor, the Zeeman effect leads to a shift in the Cooper pair energy rather than the dissolution of the pair. This occurs as the triplet pair can align with the magnetic field and thus both partners experience a symmetric interaction. In a pure p-wave material this would lead to a suppression of pair breaking in a parallel magnetic field [2]. Given a mixed s-wave/p-wave order parameter some fraction of Cooper pairs are still paired in singlets and thus the superfluid density would still decrease but more gradually than in a pure s-wave configuration providing a qualitative expectation for the results.

VII. RESONATOR PHYSICS

Throughout this thesis superconducting half-wavelength, coplanar waveguide resonators (CPWs) are utilized as a probe into the superfluid properties of the cooper pair condensate. CPWs are ideal for creating transmission line resonators due to their highly tunable properties based in large part on the geometry of the structure. Their planar nature allows for simple fabrication based on a single metallic layer removing complexity and aiding in reproducibility.

A. Coplanar Waveguide Resonators

CPWs are composed of a central strip of width w isolated from the ground planes by gaps s on both sides. These dimensions along with the resonator length ℓ and film thickness t define the geometric constraints. The designed CPW is hanger coupled to another coplanar waveguide that acts as a feedline. The scattering matrix describes voltage relationships between ports through:

$$S_{ij} = \frac{V_i^-}{V_j^+} \tag{20}$$

Transmission (S_{21}) is thus found by driving port 1 and measuring the relative voltage at port 2.

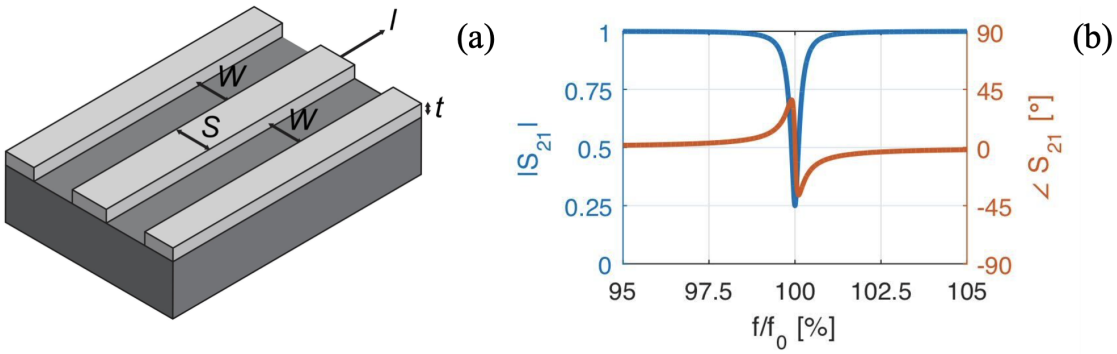

Fig. 6: (a) Diagram illustrating the spacing and central pin of the CPW [7], (b) expected S_{21} magnitude and phase response at the resonant frequency [18].

B. Resonant Frequency

The resonant frequency of a CPW has two main contributions; the geometric and kinetic resonant frequencies added in inverse quadrature [19]:

$$\frac{1}{f_r^2} = \frac{1}{f_{\text{geo}}^2} + \frac{1}{f_{\text{kin}}^2} \tag{21}$$

The geometric resonant frequency is determined from the geometric inductance and capacitance:

$$f_{\text{geo}} = \frac{1}{2\ell\sqrt{L_g C_g}} \tag{22}$$

Which are only dependent on the geometry through $k = s/(s+2w)$ and $k' = \sqrt{1-k^2}$, with K the complete elliptical integral of the first kind [20]:

$$L_g = \frac{\mu_0}{4}\frac{K(k')}{K(k)} \quad , \qquad C_g = 4\varepsilon_0\varepsilon_{\text{eff}}\frac{K(k)}{K(k')} \tag{23}$$

C. Kinetic Inductance

The kinetic resonant frequency is in turn dependent on the kinetic inductance through:

$$f_{\text{kin}} = \frac{1}{2\ell\sqrt{L_k C_g}} \tag{24}$$

The kinetic resonant frequency, and thus total resonant frequency, will shift in response to pair breaking as the kinetic inductance is inversely related to the superfluid density. Therefore, by measuring the resonant frequency as a function of temperature and the magnetic field it becomes possible to extract information about the superconductor by fitting the behaviour.

D. Resonance Bending

For small changes in frequency and temperatures far below T_c the change in resonant frequency can be approximated as in [21], [7]:

$$\frac{\Delta f_r}{f_r} = -\frac{1}{2}\frac{\Delta L_k}{L_k} = \frac{1}{2}\frac{\Delta T_c}{T_c} \tag{25}$$

Substituting the expression for pair breaking due to a parallel magnetic field, equation 17, allows for the change in resonant frequency to be expressed in terms of a quadratic field dependence:

$$\frac{\Delta f_r}{f_r} = -k_{\parallel} B_{\parallel}^2 , \qquad \text{with} \qquad k_{\parallel} = \frac{\pi}{48}\left(\frac{e^2 d^2}{\hbar k_B T_c}\right) D_{\parallel} \tag{26}$$

Likewise, pair breaking due to perpendicular field, equation 18, can be expressed as:

$$\frac{\Delta f_r}{f_r} = -k_{\perp} B_{\perp} , \qquad \text{with} \qquad k_{\perp} = \frac{\pi}{8}\left(\frac{e}{k_B T_c}\right) D_{\perp} \tag{27}$$

The frequency shift associated with magnetic impurities in a parallel field can also be given as:

$$\frac{\Delta f_r}{f_r} = -k_{imp} B_{\parallel}^2 , \qquad \text{with} \qquad k_{imp} = \frac{\pi}{16}\left(\frac{e^2 \hbar}{m^2 k_B T_c}\right) \tau_{so} \tag{28}$$

The electron diffusion constants are labelled with subscripts to indicate their origin.

VIII. METHODS

A. Resonator Design and Motivation

The geometry of the CPW resonator was iterated several times before reaching a final design due to fabrication and impedance matching constraints. Impedance matching to external electronics is essential to minimize reflection and loss. The characteristic impedance is calculated from the geometry constraining the feedline dimensions:

$$Z_0 = \sqrt{\frac{L_g}{C_g}} \tag{29}$$

This led to the selection of a central pin width $s = 20\mu$m and spacing $w = 13\mu$m for the feedline. The dimensions were designed as $\ell \approx 9$mm, $s = 25\mu$m and $w = 16\mu$m to align the geometric resonant frequency within the measurement band of the vector network analyzer.

B. Chip Fabrication

A transport device was co-fabricated on the chip to measure the critical temperature and normal state resistance. The CPW, transport device and ground plane are fabricated from a heterostructure consisting of a 5nm Ti adhesion layer and a 50nm Nb superconducting layer. The adhesion layer is necessary to ensure the Nb adheres to the silicon substrate during liftoff.

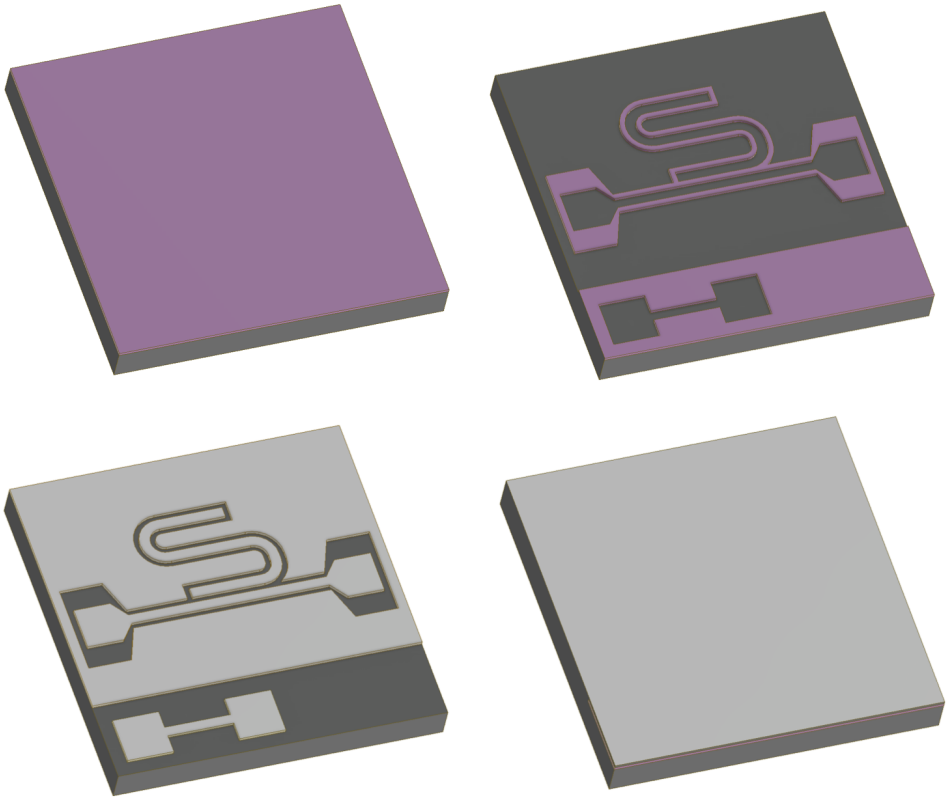

Fig. 7: (a) Spin-coating PMMA to act as a resist, (b) electron beam lithography to define the structures and developing to remove exposed resist, (c) electron beam evaporation of Ti and Nb to form the heterostructure, (d) liftoff to selectively remove metal based on the remaining resist.

The chip fabrication process is a typical liftoff procedure consisting of a series of processing steps summarized in figure 7 and detailed in the appendix. Chiral molecule adsorption is achieved through submersion in a dilute solution for 24 hours to form a self-assembled monolayer.

C. Experimental Setup

The chips were fixed to a copper bracket to ensure thermalization and bonded to a PCB to route electrical and microwave signals. The transport device was bonded in a 4 probe configuration and the feedline ports were bonded to SMP connectors to allow for measurements of S_{21} transmission. The resonator ground plane was also grounded to the PCB to alleviate any trapped modes. The chips were then connected to a puck to allow for further signal routing and loaded into an Oxford Triton dilution refrigerator. The dilution refrigerator is capable of cooling the sample to $T \simeq 8mK$ through the use of a circulating ^{3}He/^{4}He mix and is equipped with magnets with a range of 9T.

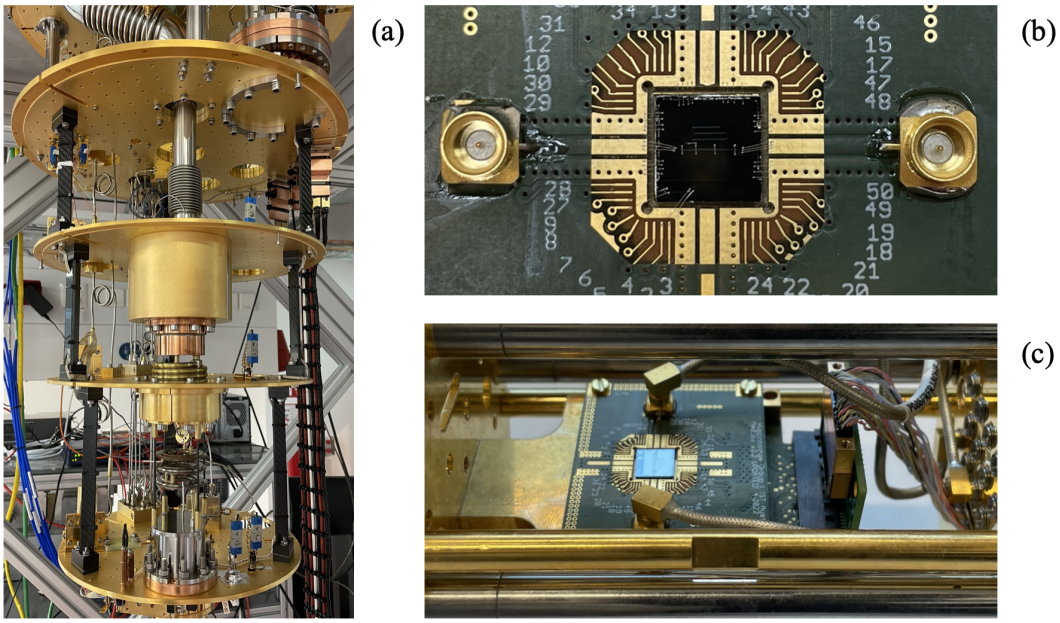

Fig. 8: (a) Dilution refrigerator, (b) picture of a bonded chip, (c) chip connected through the puck.

D. Measurement Techniques

Three main methods for gathering data were utilized to characterize the devices:

1) The transport device was connected to a lock-in amplifier allowing for the differential resistance to be measured.
2) The feedline was connected to a vector network analyzer allowing for measurements of the scattering matrix and thus transmission characteristics.
3) A ruthenium oxide thermometer inside the dilution refrigerator allowed for the temperature of the device to be determined at cryogenic temperatures.

Four types of sweeps were also used from which the shifting device response could be determined:

1) Cooldown: The temperature was swept from high temperatures in order to cool the chip to cryogenic conditions after loading.
2) Temperature Up-Sweep: The temperature was swept through in-situ heating of the device using a PID controller.
3) Parallel Field Sweep: The magnet's B_z field is aligned parallel to the chip and swept to determine a parallel pair breaking response.
4) Perpendicular Field Sweep: The magnet's B_y field is aligned perpendicular to the chip and swept to determine a perpendicular pair breaking response

IX. RESULTS

A. Molecule Adhesion and Agglomeration

In order to ensure the adhesion of molecules to the resonator, several experiments were undertaken using periodic arrays of windows in a PMMA resist as in [22]. The PMMA layer is used as a mask to allow for selective molecule adsorption to the Nb that persists after the removal of the resist. Atomic force microscopy (AFM) can then be used to measure the topography of the metal and determine the profile of the adsorbed layer as illustrated in figure 9.

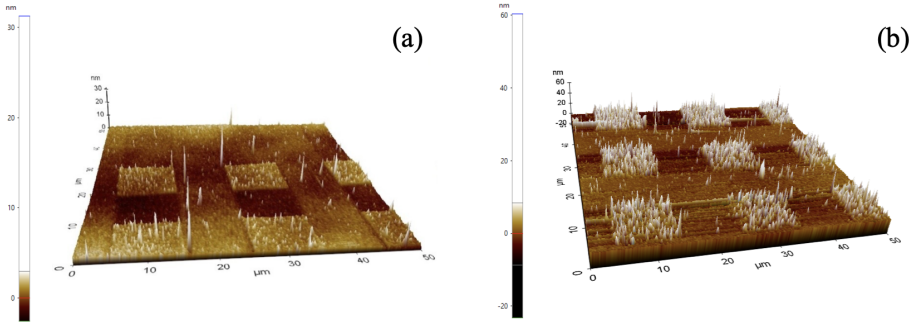

Fig. 9: (a) AFM measurements for solution 1. (b) AFM measurements for solution 2.

Two different solutions of chiral molecules were utilized in this thesis denoted as sol 1 and sol 2. The molecules from sol 1 formed a semi-homogeneous layer of around 4nm in accordance with similar results from [23]. The molecules from sol 2 formed an inhomogeneous layer characterized by large spikes in the measured height up to 40nm. These features are presumed to be molecular agglomerations indicating the molecules may not have formed a self-assembled monolayer.

B. Transport Device Measurements

The normal state resistance and critical temperature could be experimentally determined from the transport device with a lock-in amplifier. A typical temperature sweep from 20K is illustrated in figure 10 (a) and the resistance around the critical temperature in (b).

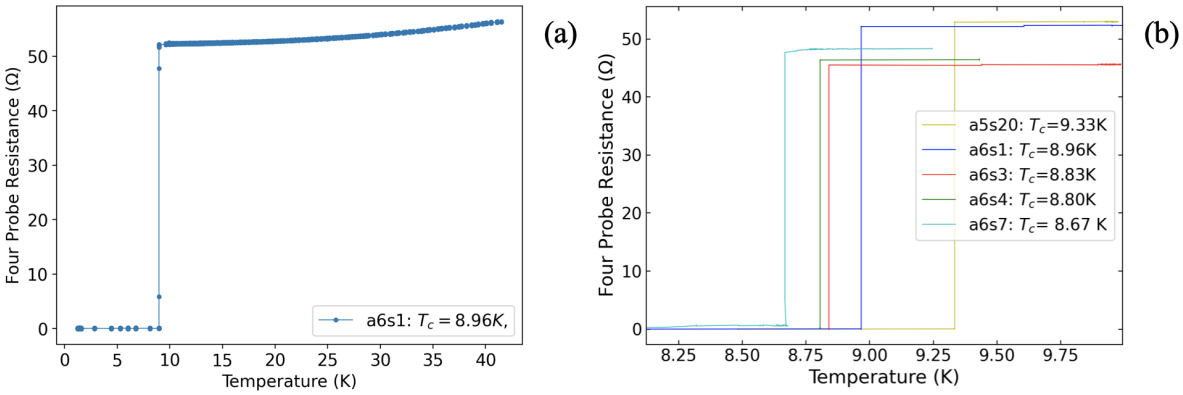

Fig. 10: (a) Typical cool-down curve illustrating the critical temperature, (b) resistance around the critical temperature.

The normal state resistance R_n was defined by the resistance before the superconducting transition with the sheet resistance determined from the width and length of the transport device:

$$R_{\square} = \frac{R_n W}{L} \tag{30}$$

All extracted values from the transport device are listed in table 10 in the appendix.

C. Transmission Measurements

The S_{21} transmission spectrum of a typical device is shown in figure 12 (a) and is characterized by a resonant frequency of 6.21 GHz with a single dominant mode.

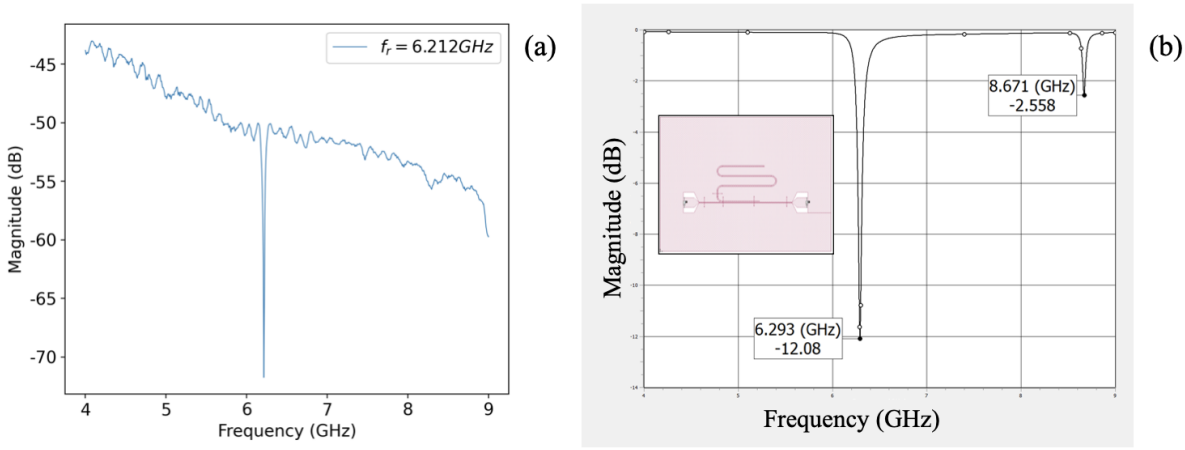

Fig. 11: (a) Typical S_{21} spectra of the 5 bond configuration, (b) sonnet simulation of 5 bond configuration.

To quantify the geometric contribution the electromagnetic properties were simulated in Sonnet and calculated with equation 22. This yielded values of $f_{geo} = 6.29$ GHz and $f_{geo} = 6.37$ GHz indicating the presence of a kinetic contribution at zero temperature and zero field.

D. Spurious Modes

In order to investigate the role of the bonding configuration on spurious modes in the transmission spectra, the same device was loaded without the final on-chip bond across the resonator. The electromagnetic properties were also simulated with Sonnet to provide a theoretical comparison.

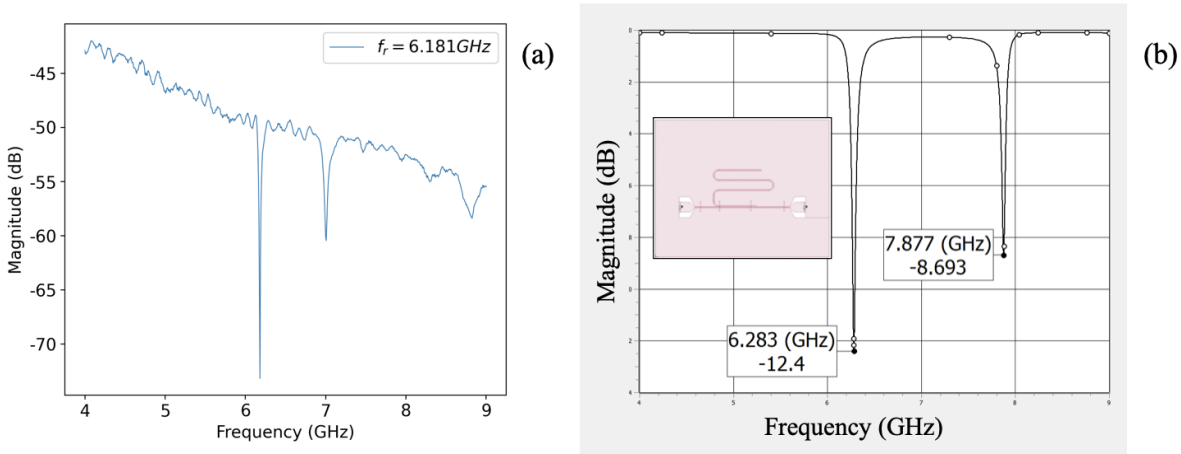

Fig. 12: (a) Experimental S_{21} spectra of the 4 bond configuration, (b) sonnet simulation of 4 bond configuration.

In the 4 bond configuration, figure 12, a spurious mode appears in the experimental and simulated transmission spectra that disappears with the additional bond across the resonator, figure 11. This can potentially be attributed to the appearance of a slot line mode along the resonator or a mode in the ground plane [24]. While the frequency of the mode in the measured spectrum is shifted from the simulation, its transience with the bonding configuration indicates that it originates from the same effect. In general, on-chip bonds allow for the creation of a continuous ground plane and alleviation of spurious modes motivating their use for the remaining devices in the 5 bond configuration.

E. Resonant Frequency vs. Temperature

The decrease in superfluid density due to temperature-dependent pair breaking is illustrated in figure 13 (a) through the movement of the resonant frequency. Performing a scan of S_{21} transmission at each temperature point yields a typical S_{21} vs. temperature sweep, 13 (b).

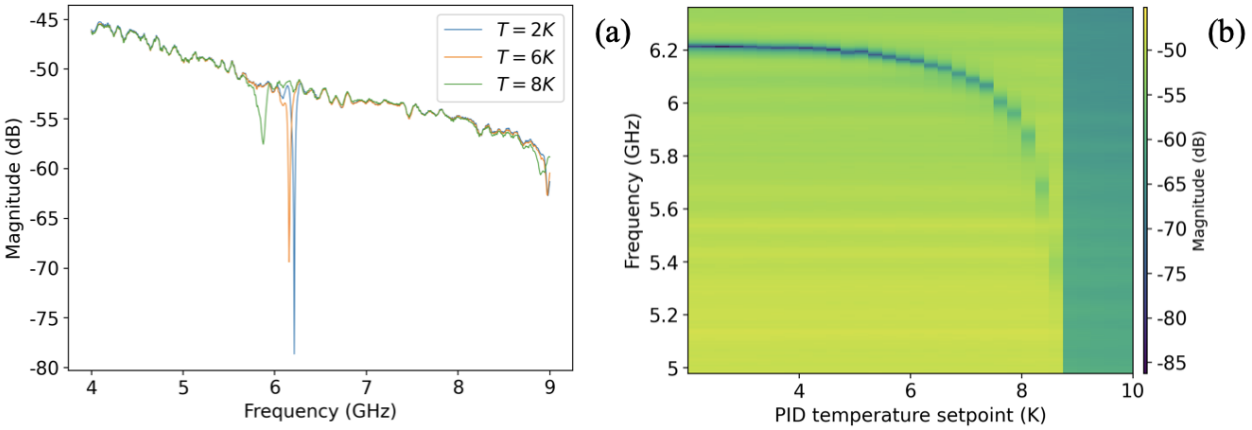

Fig. 13: (a) S_{21} scans illustrating the decrease in resonant frequency, (b) temperature sweep from 2K to 10K. (a5s20)

The resonant frequency response is characterized by a gradual decrease up to 6K followed by a rapid drop until the critical temperature. This behaviour can be attributed to the temperature-dependent increase in f_{kin} through $L_k(T)$, in turn lowering the resonant frequency. Once the critical temperature is reached the film reverts to a normal state providing an additional measurement of T_c. However, as the critical temperature derived from the transport device has more temperature steps it yields more accurate results and was thus used for the fitting procedure.

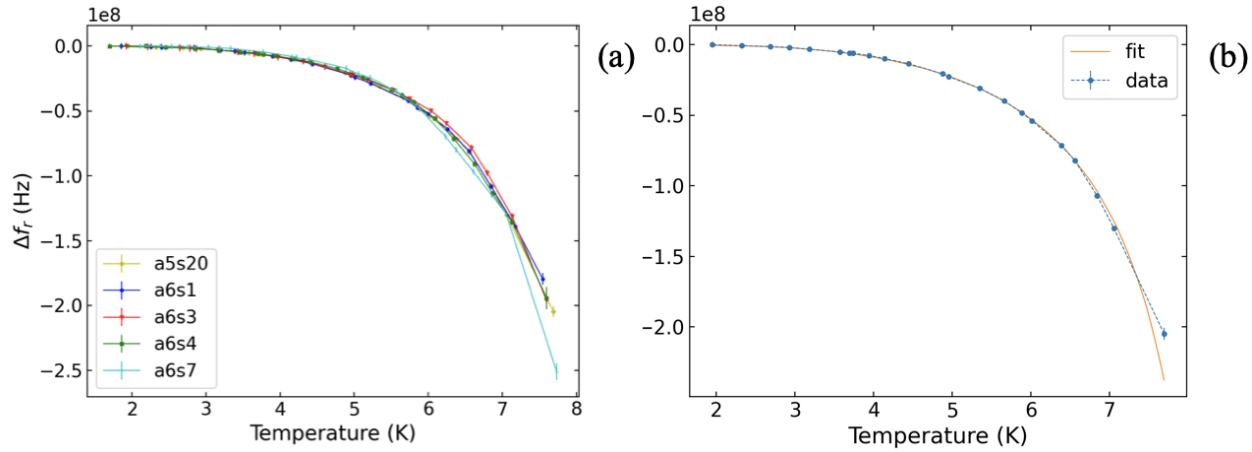

Fig. 14: (a) Temperature sweep data for all devices, (b) typical BCS fit to the resonant frequency vs. temperature data.

The temperature-dependent resonant frequency can be fit to BCS theory through equations 15 and 21. By constraining T_c the fit can be used to extract values for the geometric and kinetic resonant frequencies of each device. The extracted values for f_{geo} are in close accordance with the theoretical values calculated from the geometry indicating an accurate fit to BCS theory. The large values for f_{kin} correspond to a small contribution from kinetic inductance indicating that the resonant frequency is dominated by the geometric component. A large kinetic inductance is optimal for studying pair breaking as the corresponding shift in resonant frequency is larger and thus the sensitivity of the resonator is improved.

F. Resonant Frequency vs. Parallel Field

A typical S_{21} transmission versus parallel field sweep is illustrated in figure 15 (a). In response to a parallel field, the resonance follows a quadratic descent until reaching the lower critical field H_{c1}. The observed decrease in frequency can be attributed to pair breaking due to the Zeeman effect breaking time-reversal symmetry and subsequently destabilizing Cooper pairs.

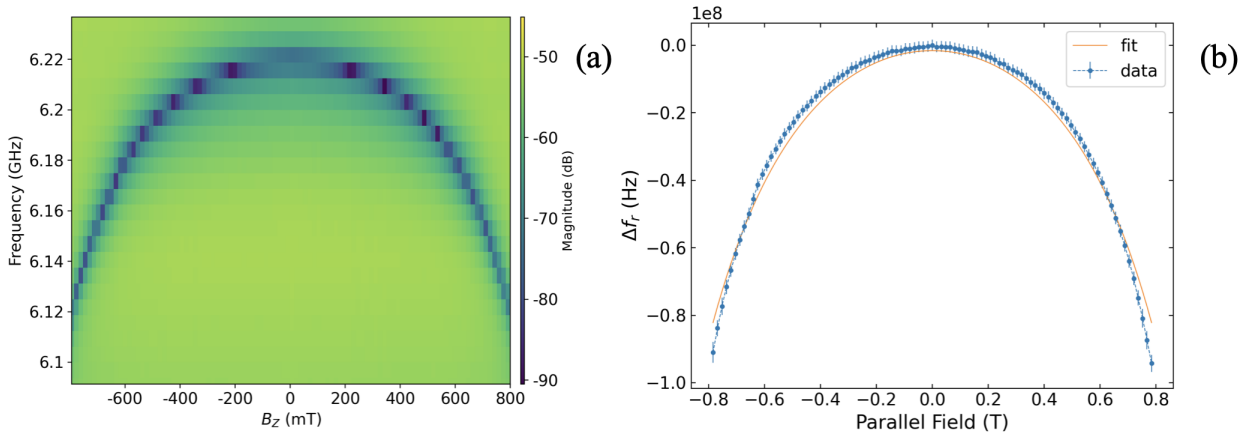

Fig. 15: (a) Parallel field sweep of S_{21} from 0.8T to -0.8T, (b) extracted resonant frequencies and parallel field fit. (a5s20)

The change in resonant frequency can be fit to the BCS pair breaking response described by equation 26. The geometric and kinetic resonant frequencies extracted from the temperature sweep are used to constrain the resonance fit and determine a value for the curvature $k_{||}$. The electron diffusion constant $D_{||}$ is then extracted from $k_{||}$ and displayed in table IV. The parallel field sweeps used in this analysis were defined within H_{c1} to avoid asymmetries in the data that would lead to systematic errors while fitting.

G. Resonant Frequency vs. Perpendicular Field

A typical S_{21} transmission versus perpendicular field sweep is illustrated in figure 16 (a). The perpendicular field response differs substantially from the parallel response with a nearly linear frequency shift. This occurs as in the perpendicular configuration the orbital term in the pair breaking coefficient dominates the contribution from the Zeeman effect. Fitting equation 18 yields a value for $k_{\perp}$ from which the electron diffusion constant $D_{\perp}$ can be extracted. As the response is not perfectly linear systematic errors exist in the fit and thus the perpendicular diffusion constant.

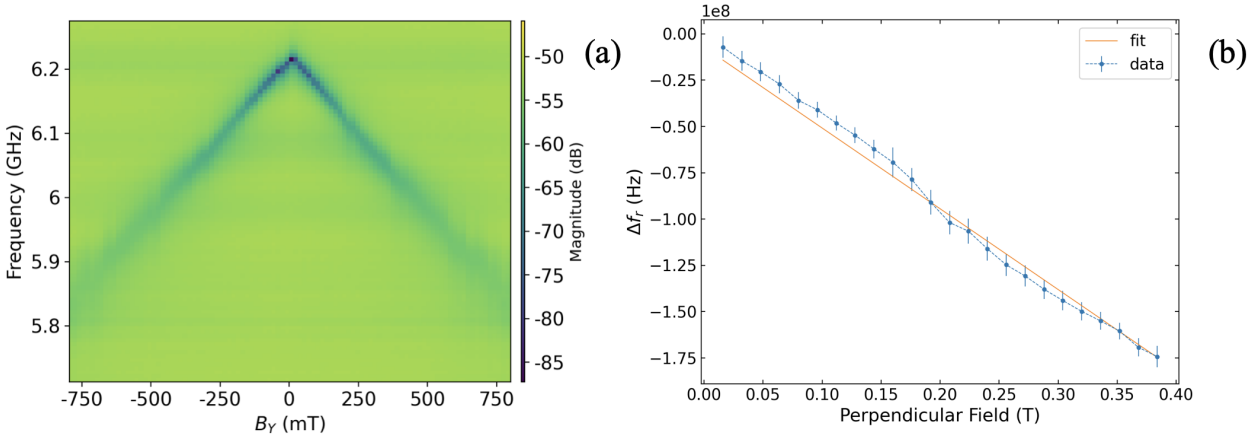

Fig. 16: (a) Perpendicular field sweep of S_{21} from 0.8T to -0.8T, (b) resonant frequencies and perpendicular field fit. (a5s20)

H. Field Dependence Comparisons

Figures 17 (a) and (b) detail the parallel and perpendicular field dependencies of the resonant frequency for devices a6s3 (sol 2), s6s4 (sol 2), and s6s7 (control). The final chip in batch 2, a6s5 (sol 1), could not be fit due to strong fluctuations in the resonant frequency with the relevant data in the appendix. The parallel diffusion constants from batch 1 (a5s20, a6s1) differ dramatically from those of batch 2 due to the different curvature and are thus not included in the comparison.

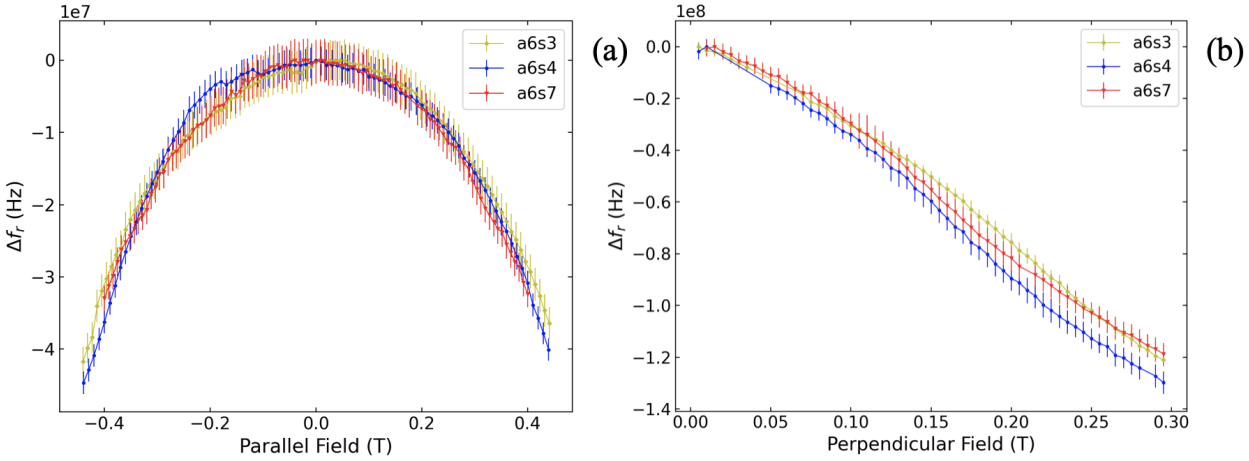

Fig. 17: (a) Parallel field data from 0.45T to -0.45T, (b) perpendicular field data from 0.3T to -0.3T.

Comparing the parallel and perpendicular responses reveals similar behaviour with and without adsorbed molecules. If the molecules can be modelled as magnetic impurities an additional shift would be expected in the parallel field data. Under the influence of a parallel field, magnetic impurities provide an additional pair-breaking term with a quadratic field dependence. While this term is present in the perpendicular field its contribution is dominated by the linear term and can thus be neglected. Using $D_\perp$ in the expression for $k_\parallel$ yields a corrected curvature for the parallel field fit k_{cor}. The resulting shift in resonant frequency would then be expressed as:

$$\frac{\Delta f_r}{f_r} = k_\parallel H_\parallel^2 = (k_{cor} + k_{imp}) H_\parallel^2 \implies k_{imp} = k_\parallel - k_{cor} \tag{31}$$

Ideally, the expression for k_{imp} can then be used to extract the scattering time due to the magnetic impurities τ_{so}. The values of $D_\parallel$ for the three devices of batch 2 illustrate an issue with normalization with $D_\parallel \approx 20 D_\perp$ as detailed in table II, to compare the values the ratio is taken instead. Given the small shift and large systematic errors in the fits, no definitive result can be determined on if there was a shift in the parallel field response.

TABLE II: Extracted diffusion constants from the parallel and perpendicular fits from batch 2.

Chip	$D_\parallel$ (cm$^{-2}/s$)	$D_\perp$ (cm$^{-2}/s$)	$D_\parallel/D_\perp$
a6s3 (sol 2)	20.79	1.15	18.04
a6s4 (sol 2)	24.15	1.31	18.41
a6s5 (sol 1)	–	–	–
a6s7 (control)	24.07	1.24	19.44

The response of a6s5 (sol 1) differs from the other chips with fluctuations in frequency under applied field and lossy transmission at resonance.

I. Hysteresis in Field

When the parallel magnetic field exceeded a certain threshold value on the up-sweep B_{th1} the pair-breaking response deviated from the expected quadratic behaviour. On the down-sweep, a corner also appears in the frequency response at B_{th2}. The values of these thresholds are symmetric when reversing the sweep direction as illustrated in figure 18.

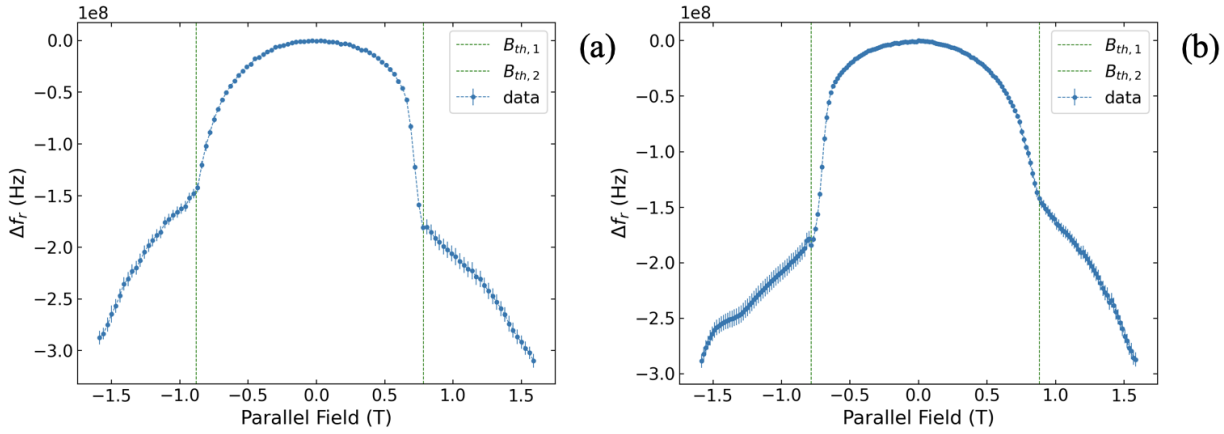

Fig. 18: (a) Parallel field sweep from 1.6T to -1.6T, (b) parallel field sweep from -1.6T to 1.6T, a5s20 (control batch 1).

The deviation from quadratic behaviour may occur in response to the formation of vortices in the type two superconductor with the threshold value B_{th1} corresponding to the lower critical field B_{c1}. It should be noted that B_{th1} and B_{th2} are not symmetric around $B = 0$ with $B_{th1} < B_{th2}$. The shift in the resonant frequency around B_{th1} is much more gradual than around B_{th2} at which the slope increases dramatically for a few hundred MHz before rapidly flattening out. This flattening may correspond to the re-expulsion of magnetic flux by the Meissner effect. The two batches of devices demonstrate different values for the threshold fields but the same overall response with a control device from batch 2 illustrated in figure 19.

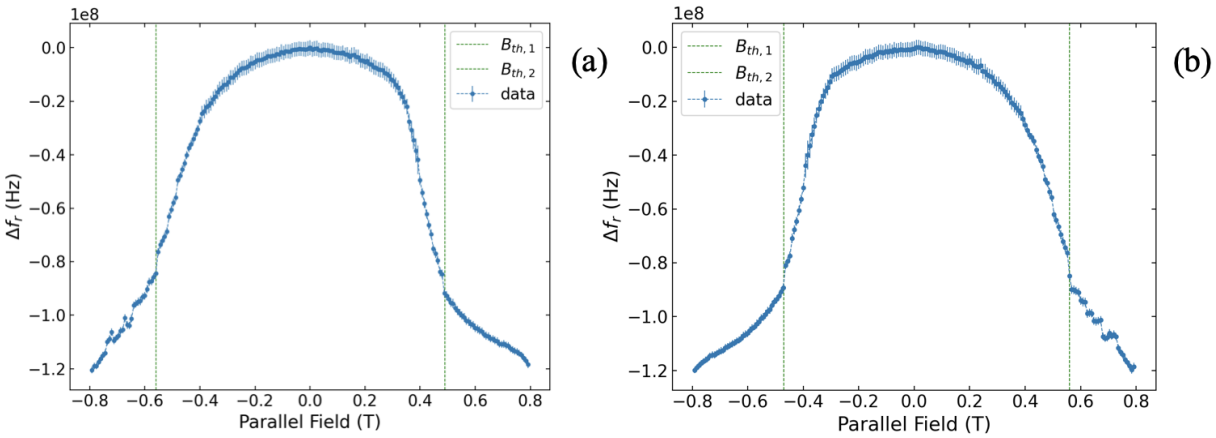

Fig. 19: (a) Parallel field sweep from 0.8T to -0.8T, (b) parallel field sweep from -0.8T to 0.8T, a6s7 (control batch 2).

The role of molecules in this behaviour is unclear with the control and sol 2 devices behaving similarly. The response of a6s5 (sol 1) also displays the threshold fields 22 despite the fluctuations.

J. Temperature Sweeps with $T \ll T_c$

The low-temperature frequency response of a device with molecules from sol 2 is illustrated in figure 20 (b) in terms of the kinetic inductance. The BCS prediction for the device, figure 20 (a) is extracted from the corresponding 2K-10K temperature sweep BCS fit.

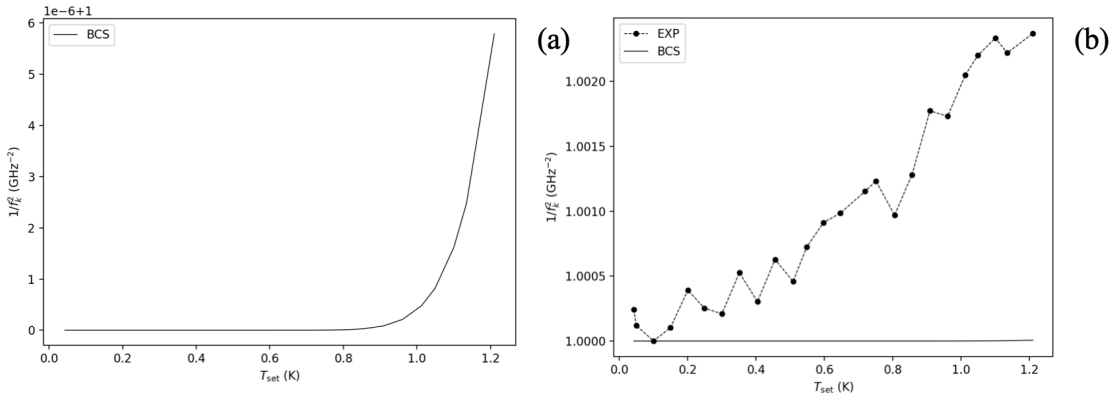

Fig. 20: (a) BCS prediction for the low-temperature response of the kinetic inductance, (b) experimental shift in the kinetic inductance from a sweep of 0K-1.2K.

The low-temperature kinetic inductance response naively indicates a deviation from BCS theory. Due to the very slight shift and systematic errors in the resonance fitting function of the same order of magnitude, this result cannot be definitively relied on. Rather, the shift can be extracted more systematically from the phase response. Figure 21 illustrates the extracted phase shift around the resonant frequency at different temperatures.

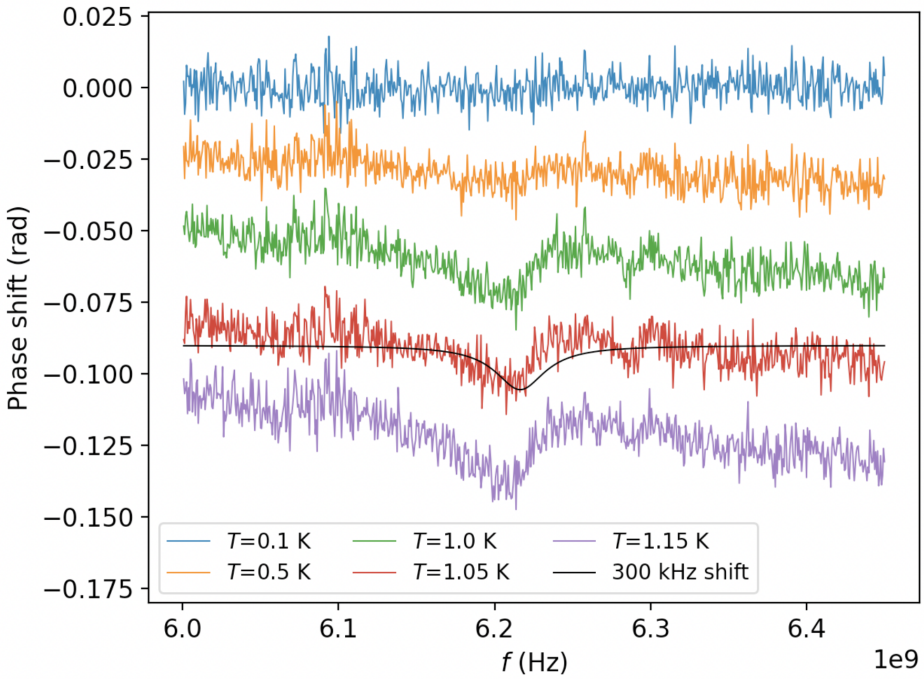

Fig. 21: Relative phase shift around the resonant frequency over cuts of the temperature sweep.

When increasing temperature a phase shift can be determined at resonance of approximately 300kHz. While this can not be decisively linked to the presence of molecules, due to the lack of control data, it does illustrate a deviation from BCS theory.

X. DISCUSSION

In this thesis, the pair-breaking response of Nb resonators with and without adsorbed chiral molecules was experimentally investigated through temperature, parallel field, and perpendicular field sweeps. Specifically, the electron diffusion constant was extracted through independent measurements of the resonant frequency's response to parallel and perpendicular magnetic fields. Due to the small shift upon molecule adsorption a definitive answer on if the molecules contribute an additional term to pair breaking could not be determined. Therefore, it remains unclear if chiral molecules can be modelled as magnetic impurities in a conventional superconductor.

The adsorption of chiral molecules from sol 1 appeared more indicative of the formation of a self-assembled monolayer than adsorption from sol 2. The AFM profile of sol 2 exhibited peaks far higher than sol 1 possibly due to molecular agglomerations. Values for D could not be determined for the chip from sol 1 due to large fluctuations in the resonant frequency. Therefore, a shift may have occurred but the utilized technique is insufficient to resolve it. More research is needed on the nature of the fluctuations and if they originate from the adsorbed chiral molecules.

The hysteretical behaviour at high magnetic fields indicates the presence of vortices in the devices and thus the potential that additional phenomena may be at play. The shifting lower critical field from batch to batch also demonstrates inconsistency in the fabrication or the contamination of devices. Both results demonstrate the importance of addressing vortex formation and behaviour in order to definitively claim if an effect arises due to a proximity effect with the chiral molecules.

The critical temperature and normal state resistance were also measured from a co-fabricated transport device. The critical temperature appeared to shift between batches with devices from batch 1 having higher critical temperatures than devices from batch 2. Paired with the decrease in the lower critical field for batch 2 this could indicate a closing of the superconducting gap due to contamination during fabrication.

Finally, the low-temperature response for a resonator with adsorbed chiral molecules was experimentally measured. The experiment illustrated a deviation from BCS theory with a shift in the resonant frequency of several hundred kHz. This low-temperature response could indicate the emergence of triplet pairing in the superconductor but due to the lack of control data, this result is inconclusive. The low-temperature deviation could also indicate a general deviation from BCS theory for thin-film Type 2 superconductors and not due to adsorbed chiral molecules. More data is needed to verify this result and determine the underlying mechanism.

XI. CONCLUSION AND FUTURE OUTLOOK

The pair breaking and low-temperature responses of Nb coplanar waveguide resonators were investigated in order to probe the nature of adsorbed chiral molecules on type 2 superconductors. The results of this study proved inconclusive with observed changes in the pair breaking response and a low-temperature frequency shift but also additional effects that complicated the picture making substantive claims difficult. More data is required before any concrete results can be attributed to the interaction. There are several key points for improvement that could assist in providing definitive answers to the research questions laid out above. In order to improve the resonant frequency's sensitivity to shifts in the superfluid density, the kinetic inductance of the device should be increased. This can be accomplished by using a different material such as NbTiN or decreasing the thickness of the films. The complexity introduced by vortex dynamics should also be minimized as much as possible. One way of doing so is by patterning an array of artificial defect sites in the ground plane to trap vortices. Combining the two suggestions may lead to highly sensitive resonators that are resilient to vortex formation and movement allowing for more accurate measurements of the shift in resonant frequency to be taken.

REFERENCES

[1] S. Ran, C. Eckberg, Q.-P. Ding, *et al.*, "Nearly ferromagnetic spin-triplet superconductivity," *Science*, vol. 365, no. 6454, pp. 684–687, 2019.

[2] J. Linder and J. W. Robinson, "Superconducting spintronics," *Nature Physics*, vol. 11, no. 4, pp. 307–315, 2015.

[3] J. F. Annett *et al.*, *Superconductivity, superfluids and condensates*. Oxford University Press, 2004, vol. 5.

[4] M. Tinkham, *Introduction to superconductivity*. Courier Corporation, 2004.

[5] J. Bardeen, L. N. Cooper, and J. R. Schrieffer, "Theory of superconductivity," *Physical review*, vol. 108, no. 5, p. 1175, 1957.

[6] C. Kittel and P. McEuen, *Introduction to solid state physics*. John Wiley & Sons, 2018.

[7] J. Kroll, F. Borsoi, K. Van Der Enden, *et al.*, "Magnetic-field-resilient superconducting coplanar-waveguide resonators for hybrid circuit quantum electrodynamics experiments," *Physical Review Applied*, vol. 11, no. 6, p. 064 053, 2019.

[8] D. Bothner, C. Clauss, E. Koroknay, *et al.*, "Reducing vortex losses in superconducting microwave resonators with microsphere patterned antidot arrays," *Applied Physics Letters*, vol. 100, no. 1, p. 012 601, 2012.

[9] A. Mackenzie and Y. Maeno, "P-wave superconductivity," *Physica B: Condensed Matter*, vol. 280, no. 1-4, pp. 148–153, 2000.

[10] Y. Tanaka, Y. Tanuma, K. Kuroki, and S. Kashiwaya, "Theory of magnetotunneling spectroscopy in spin triplet p-wave superconductors," *Journal of the Physical Society of Japan*, vol. 71, no. 9, pp. 2102–2105, 2002.

[11] E. Talantsev, K. Iida, T. Ohmura, *et al.*, "P-wave superconductivity in iron-based superconductors," *Scientific reports*, vol. 9, no. 1, pp. 1–13, 2019.

[12] X. Yang, "Connecting chirality and spin in electronic devices," Ph.D. dissertation, University of Groningen, 2020.

[13] H. Alpern, E. Katzir, S. Yochelis, N. Katz, Y. Paltiel, and O. Millo, "Unconventional superconductivity induced in nb films by adsorbed chiral molecules," *New Journal of Physics*, vol. 18, no. 11, p. 113 048, 2016.

[14] H. Alpern, M. Amundsen, R. Hartmann, *et al.*, "Unconventional meissner screening induced by chiral molecules in a conventional superconductor," *Physical Review Materials*, vol. 5, no. 11, p. 114 801, 2021.

[15] H. Alpern, K. Yavilberg, T. Dvir, *et al.*, "Magnetic-related states and order parameter induced in a conventional superconductor by nonmagnetic chiral molecules," *Nano Letters*, vol. 19, no. 8, pp. 5167–5175, 2019.

[16] B. Gunupudi, "Coupled superconducting microwave resonators for studies of electromechanical interaction," Ph.D. dissertation, University of Birmingham, 2015.

[17] A. J. Annunziata, D. F. Santavicca, L. Frunzio, *et al.*, "Tunable superconducting nanoinductors," *Nanotechnology*, vol. 21, no. 44, p. 445 202, 2010.

[18] T. Boehme, "Characterisation and optimisation of superconducting microwave resonators," M.S. thesis, 2016.

[19] D. Phan, J. Senior, A. Ghazaryan, *et al.*, "Detecting induced p$\pm$i p pairing at the al-inas interface with a quantum microwave circuit," *Physical Review Letters*, vol. 128, no. 10, p. 107 701, 2022.

[20] M. Göppl, A. Fragner, M. Baur, *et al.*, "Coplanar waveguide resonators for circuit quantum electrodynamics," *Journal of Applied Physics*, vol. 104, no. 11, p. 113 904, 2008.

[21] N. Samkharadze, A. Bruno, P. Scarlino, *et al.*, "High-kinetic-inductance superconducting nanowire resonators for circuit qed in a magnetic field," *Physical Review Applied*, vol. 5, no. 4, p. 044 004, 2016.

[22] O. Ben Dor, S. Yochelis, A. Radko, *et al.*, "Magnetization switching in ferromagnets by adsorbed chiral molecules without current or external magnetic field," *Nature communications*, vol. 8, no. 1, pp. 1–7, 2017.

[23] T. Shapira, H. Alpern, S. Yochelis, *et al.*, "Unconventional order parameter induced by helical chiral molecules adsorbed on a metal proximity coupled to a superconductor," *Physical Review B*, vol. 98, no. 21, p. 214 513, 2018.

[24] G. E. Ponchak, J. Papapolymerou, and M. M. Tentzeris, "Excitation of coupled slotline mode in finite-ground cpw with unequal ground-plane widths," *IEEE transactions on microwave theory and techniques*, vol. 53, no. 2, pp. 713–717, 2005.

APPENDIX

A. Chip Fabrication

The chips used in this thesis were fabricated according to a typical liftoff procedure consisting of the following steps:

1) Chip design: The chips were designed using AutoCAD from which the write fields could be determined using the software Beamer. The resulting GPF files were used to define the dosing pattern for electron beam lithography.

2) Cleaning the substrate: The substrates were cleaned through sonication in IPA for 4 minutes at power 4 followed by sonication in acetone for 4 minutes at power 4. They were then dried with nitrogen and pre-baked at 170°C for 3 minutes.

3) Spin-coating the resist: Two drops of the resist PMMA 950K 4% were deposited on the substrate before spin-coating with a speed of 4000 rpm, acceleration of 1500 rpm/s and time of 60s. After spin-coating, the substrates were baked at 170° for 3 minutes.

4) Electron beam lithography: Using the GPF files the resist was patterned using electron beam lithography to define the ground plane, feedline/resonator and transport device.

5) Developing the resist: The exposed resist was developed using a 3:1 solution of IPA and deionized water for 90s. Developing was halted by submerging the chips in a solution of IPA for 30s.

6) Electron beam evaporation: The chips were then transferred to an ultra-high vacuum electron beam evaporator. The evaporation chamber was pumped down to 10^{-9} bar through the use of Titanium gettering before a 5nm layer of Titanium was deposited. A 50nm layer of Niobium was then deposited on the substrate.

7) DMSO based liftoff: The unexposed resist was then lifted off by submerging the chips in a DMSO bath at 40°C for 30 minutes.

8) Molecule adsorption: In order to adsorb the chiral molecules to the Nb resonators they were submerged in a 1mM solution of polyalanine alpha-helix molecules dissolved in ethanol for 24 hours.

After adsorption, the chips were cleaned to remove molecules not adsorbed to the surface. This was done by originally washing with acetone for 1 minute and ethanol for 1 minute (for a6s1). For devices from batch 2, the cleaning was shortened to just washing with ethanol for 1 minute.

B. Extracted Data from Temperature and Field Sweeps

TABLE III: Extracted geometric and kinetic resonant frequencies from the temperature fit and results from the transport device.

Chip	f_{geo} (GHz)	f_{kin} (GHz)	T_c (K)	$R_\square$ (Ω)
a5s20 (control)	$6.32 \pm 1.34 \cdot 10^{-3}$	$33.54 \pm 1.49 \cdot 10^{-1}$	9.33	1.41
a6s1 (sol 1)	$6.32 \pm 1.69 \cdot 10^{-3}$	$33.79 \pm 1.78 \cdot 10^{-1}$	8.96	1.39
a6s3 (sol 2)	$6.31 \pm 2.04 \cdot 10^{-3}$	$34.99 \pm 2.66 \cdot 10^{-1}$	8.83	1.21
a6s4 (sol 2)	$6.31 \pm 1.65 \cdot 10^{-3}$	$32.93 \pm 1.72 \cdot 10^{-1}$	8.80	1.24
a6s5 (sol 1)	–	–	9.26	1.23
a6s7 (control)	$6.31 \pm 1.71 \cdot 10^{-3}$	$32.01 \pm 1.61 \cdot 10^{-1}$	8.67	1.29

The large values for the kinetic resonant frequencies correspond to small contributions from the kinetic inductance. The geometric resonant frequency is stable and close to theoretical values.

TABLE IV: Extracted diffusion constants from the parallel/perpendicular magnetic field fits.

Chip	$D_{\parallel}$ (cm$^{-2}/s$)	$D_{\perp}$ (cm$^{-2}/s$)	$D_{\parallel}/D_{\perp}$
a5s20 (control)	$12.17 \pm 3.55 \cdot 10^{-2}$	$1.34 \pm 1.44 \cdot 10^{-2}$	9.07
a6s1 (sol 1)	$13.81 \pm 5.74 \cdot 10^{-2}$	–	–
a6s3 (sol 2)	$20.79 \pm 1.91 \cdot 10^{-1}$	$1.15 \pm 6.19 \cdot 10^{-3}$	18.04
a6s4 (sol 2)	$24.15 \pm 1.21 \cdot 10^{-1}$	$1.31 \pm 1.02 \cdot 10^{-2}$	18.41
a6s5 (sol 1)	–	–	–
a6s7 (control)	$24.07 \pm 1.72 \cdot 10^{-1}$	$1.24 \pm 1.05 \cdot 10^{-2}$	19.44

The data set for a6s1 is incomplete with the perpendicular field dependence missing. The results for a6s5 could not be fit due to large fluctuations in the resonant frequency. The associated errors are extracted during the fit.

C. Data from a6s5 (sol 1)

The device with molecules adsorbed from sol 1 in batch 2 (a6s5) was unable to be fit with the pair-breaking expressions due to fluctuations in the resonant frequency. The S_{21} response to the parallel and perpendicular field sweeps are illustrated in figure 22.

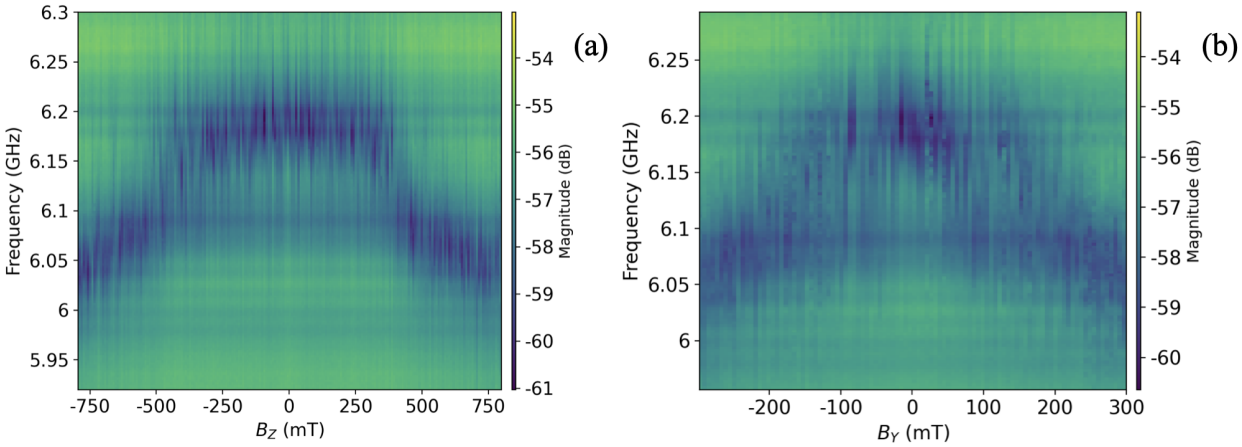

Fig. 22: S_{21} parallel and perpendicular magnetic field sweeps for a6s5.

Despite adsorption from the same solution, the data for a6s1 does not indicate any fluctuations in the resonant frequency. This may have occurred due to the after-adsorption cleaning being too intense or it may indicate the fluctuations arise due to another aspect of a6s5.

D. NbTiN Devices

Before using Niobium (Nb) as the superconducting layer, devices fabricated from Niobium Titanium Nitride (NbTiN) were utilized due to their high kinetic inductance and thus sensitivity to pair breaking. A full transmission spectrum to 14GHz is illustrated in figure 23.

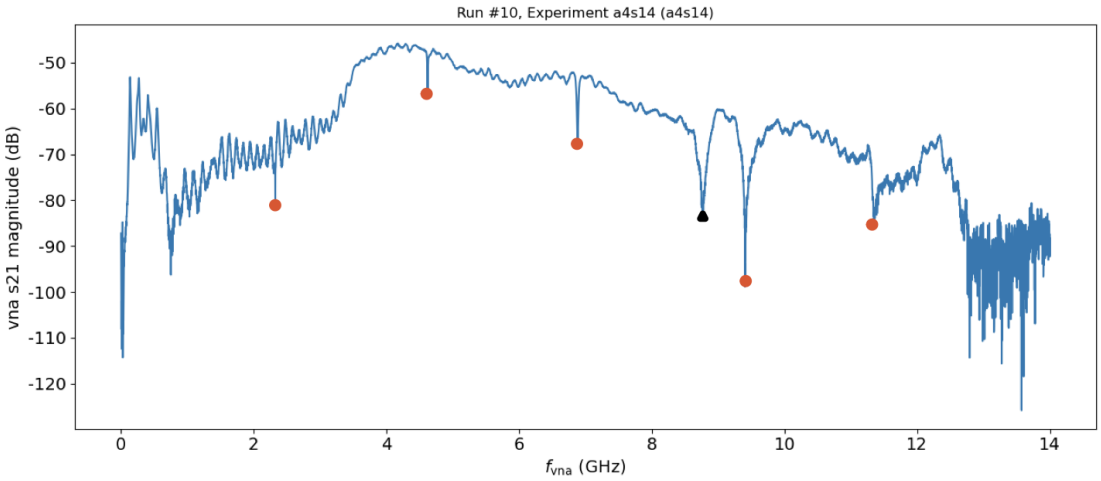

Fig. 23: S_{21} transmission spectrum of a NbTiN coplanar waveguide resonator.

In response to the high kinetic inductance, the resonant frequency was shifted out of the optimal measurement band to 2.32GHz. The higher harmonics of the resonant frequency are labelled with red circles whereas a spurious mode in the spectrum is labelled in black. Due to time constraints and the more complicated behaviour, it was decided to first measure the response of Nb resonators and then return to NbTiN